# Large eddy simulations of electrification of liquid dielectrics in channel flow

Mathieu Calero[a,1], Holger Grosshans[b] and Miltiadis V. Papalexandris[a,*]

[a]Institute of Mechanics, Materials and Civil Engineering, 1348 Louvain-la-Neuve, Belgium
[b]Physikalisch-Technische Bundesanstalt, 38116 Braunschweig, Germany

ARTICLE INFO

*Keywords*:
flow electrification
turbulent flows
dielectric liquids
large eddy simulations
electrical double layer
electrohydrodynamics

Abstract

In this paper we present a computational study of electrification of liquid dielectrics in channel flow and at moderate turbulence intensities. For purposes of computational savings this study consists of large eddy simulations, according to which the large turbulent scales are directly resolved by the computational grid while the effect of the smaller unresolved scales is suitably modeled. First we examine different subgrid-scale models for the electric charge density. Their efficacy is then assessed via comparisons with results from direct numerical simulations at low turbulence intensities. According to our comparisons and analysis, the most efficient model is the one based on the eddy diffusivity approach and the introduction of the turbulent electric Schmidt number. Subsequently, we present numerical results of electrification of benzene in channel flow and at different Reynolds numbers. Herein we discuss the various stages of the electrification process and the variation of the total charge and streaming current with the turbulence intensity. According to our findings, the increase of the turbulence intensity rises dramatically not only the amount of charge transported in the bulk of the fluid but also the rate at which this transport takes place. Finally, we present results for the statistics of the charge density, which provide additional insight about the distribution of the electric charges in the liquid.

## 1. Introduction

Flow electrification occurs when electric charges are transported from the interface between a solid boundary and a flowing liquid dielectric towards the bulk of the flow domain. The class of liquid dielectrics includes several hydrocarbons like benzene, toluene, heptane and others. In their pure state, liquid dielectrics are free of electric charges. However, they inevitably contain impurities. In turn, these impurities get dissolved into particles carrying electric charge, namely, anions and cations. These charged particles then participate in the formation of the Electrical Double Layer (EDL) at the interface between a solid boundary and the liquid dielectric. The first layer of the EDL is referred to as the surface charge and is on the side of the solid body.

The second layer is on the side of the liquid and is composed of ions attracted to the surface charge. According to the Stern model of EDL (Stern, 1924), it consists of two sublayers, the Stern and the diffuse layer. The Stern layer, whose thickness is of the order of the ion size, is anchored to the solid boundary and contains ions whose charge is opposite to that of the surface charge, so as to maintain an electrically neutral interface. On the other hand, the diffuse layer has a loose structure and the concentration of ions therein decreases away from the solid surface. Typically, the thickness of the EDL is a few Debye lengths. The Debye length is the characteristic length-scale of electrostatic effects in fluids and plasmas. It is of the order of a micron and its precise value depends on the electrical properties of the medium (Atkins et al., 2018; Berg, 2010). In particular, it is proportional to the square root of the electrical resistivity of the liquid.

Liquid dielectrics have high resistivity hence Debye length. Accordingly, the thickness of their diffuse layers is comparatively higher than in other liquids. This makes it easier for electric charges to be transported away from the diffuse layer and towards the bulk of the flow domain. In other words, a thicker diffuse layer facilitates flow electrification. However, this phenomenon leads to high streaming currents, i.e. electric currents due to the convective motions (flow) of the liquid, which constitute a major safety hazard. By now it is well documented that electric discharges caused by flow electrification of flammable dielectrics have caused many accidents in the petroleum and

*Corresponding author
miltos@uclouvain.be (M.V. Papalexandris)
ORCID(s):
[1]Present address: Université Claude-Bernard Lyon 1, Institut Camille-Jordan, 69603 Villeurbanne, France

process industries; see for example the earlier reports of Klinkenberg (1959, 1964) and the more recent account of Ohsawa (2011). Additionally, flow electrification is often responsible for the failure of power transformers (Bourgeois et al., 2005). It is also worth adding that flow electrification does not occur only in transport of liquid dielectrics in pipes and ducts but also during filtration (Huber and Sonin, 1977b,a) and flows through porous media (Gavis and Wagner, 1968; Paillat et al., 2000, 2001a).

Since flow electrification represents a major safety hazard, it has been the subject of concentrated research efforts in the past. Moreover, since the phenomenon involves convective transport of charges, it had been proposed early on that flow turbulence plays a significant role to it. For example, Gavis and Koszman (1961); Koszman and Gavis (1962a,b) provided some early theoretical and experimental studies of electrification of pipe flows. In their theoretical studies they considered the time-averaged equation for the electric charge density and derived expressions for the streaming current by invoking several simplifying assumptions and by introducing the concept of eddy diffusivity of electric charges. Twenty years later, Abedian and Sonin (1982) extended those studies and derived closed-form expression for the streaming current and the charge density by assuming a simplified profile of the streamwise velocity.

The charge distribution and streaming current inside the diffuse layer were studied theoretically and experimentally by Boumans (1957a,b,c,d). His theoretical analysis was based on the Debye-Hückel equation for the electric potential. Later on, Touchard (1978) undertook Boumans' work and expanded it. In particular, Touchard (1978) derived a closed-form solution for the charge density in the diffuse layer for a fluid at rest or in laminar flow. In the same paper, he proposed a model for the charge-density profile in turbulent flows that assumed constant charge density in the bulk of the flow; consequently, that profile was discontinuous at the edge of the diffuse layer. This was corrected later in the model of Cabaleiro et al. (2019) who proposed a continuous profile by making use of the eddy-diffusivity concept but without properly taking into account the convective transport of ions. Recently, Touchard (2021a) proposed to combine those two models by splitting the diffuse layers into two regions; in the first region tubulence does not afect the charge density distribution while the eddy-diffusivity concept is applied in the second region. Comparisons of these three models with experimental results were reported by Touchard (2021b). Additional studies on the streaming current in the diffuse layer have been provided by Domínguez and Touchard (1997), Paillat et al. (2001b) and others. Further, the study of the physico-chemical phenomena that take place at liquid-solid interfaces and the development of the diffuse layers has also been pursued by Touchard and his collaborators (Touchard et al., 1996; Cabaleiro et al., 2008; Paillat et al., 2009; Leblanc et al., 2017), based on the so-called corroding model. Additional studies on this topic have been presented, among others, by Walmsley and Woddford (1981), Washabaugh and Zhan (1997), El-Adawy et al. (2010, 2011), and Leblanc et al. (2018). The above works have provided important physical insight on the phenomenon and elucidated the role of several underpinning mechanisms. However, they all focused on the charge-density distribution in a stationary state, i.e. by assuming that the electrification process has been completed. Further, they necessarily relied on approximate expressions for the mean velocity profile in a turbulent flow. Therefore, they did not provide information about the evolution of the electrification process and, furthermore, did not quantify the role of the turbulence intensity.

In a recent paper (Calero et al., 2023), we presented a numerical study of the electrification process in turbulent channel flows at weak turbulence intensity. That study consisted of Direct Numerical Simulations (DNS), which means that the computational grid of the flow domain was sufficiently refined so as to resolve all turbulent structures and flow scales. According to our simulations, the amount of electric charge transported in the interior of the channel increases dramatically when the flow becomes turbulent. Also, the electrification rate increases with the turbulence intensity. This is due to the fact that, as the turbulence intensity increases, the thickness of the hydrodynamic boundary layer becomes comparable to that of the diffuse layer which, in turn, facilitates and enhances the convective transport of charged particles. Accordingly, electric charge is built up rapidly in the interior of the channel until it reaches a plateau, which signals the completion of the electrification process.

In the present paper, we expand upon our earlier results (Calero et al., 2023) and study numerically the electrification process at higher turbulence intensities, i.e. at higher Reynolds numbers. The grid-resolution requirements increase tremendously as the turbulence intensity increases because of the development of ever smaller flow structures (eddies). Therefore, for purposes of computational savings, the present study is based on Large Eddy Simulations (LES) instead of DNS. According to the LES approach, the computational grid is sufficiently fine to resolve the large turbulent structures of the flow-field, which are also the ones that contain most of the turbulent kinetic energy. Whereas the effect of the smaller unresolved structures is modeled. This procedure amounts to apply a spatial filter in the governing equations and then derive appropriate models for the unclosed terms.

To our knowledge, this is the first set of numerical simulations of flow electrification at moderate turbulence inten-

sities and also the first study of this phenomenon based on LES. For this reason, first we have to provide an appropriate LES (subgrid-scale) model for the charge-density equation. Herein we introduce four different subgrid-scale models for the charge-density equation and examine their performance via comparisons with DNS results. We then select the most appropriate model in terms of accuracy, robustness and ease of implementation. Subsequently, we present results from LES based on the selected subgrid-scale model.

This paper is structured as follows. In Section 2, we present the filtered version of the governing equations for the flows of interest and discuss the subgrid-scale model for the momentum equation. In Section 3 we assess the efficacy of different subgrid-scale models for the charge-density equation. Then, in Section 4, we present and discuss results from our LES of channel-flow electrification at different Reynolds numbers. Finally, section 5 concludes.

## 2. Governing equations

In the flows of interest, dynamic currents due to charge transport are very small so that electromagnetic induction is negligible. Variations of the fluid density and temperature are assumed to be negligible as well. Accordingly, the governing equations are the Navier-Stokes equations, supplemented by the transport equation for the electric charge and the Gauss law for the electric field (Calero et al., 2023). In the context of LES, the filtered version of these equations are employed. A spatially filtered field $\widetilde{\psi}$ of a generic quantity $\psi$ is given by,

$$\widetilde{\psi}(\boldsymbol{x},t) \;=\; \int \psi(\boldsymbol{x}',t)\, G(\boldsymbol{x}-\boldsymbol{x}',t)\, d\boldsymbol{x}' \,, \tag{1}$$

where $G$ represents the filter kernel associated with the cutoff scales in space. As is often the case in LES, in our study we assume that $G$ is the top hat function: it is equal to unity inside a given computational cell and zero outside. By applying the above spatial filter, we obtain the filtered version of the equations of electrohydrodynamics,

$$\nabla\cdot\widetilde{\boldsymbol{u}} \;=0\,, \tag{2}$$

$$\frac{\partial\widetilde{\boldsymbol{u}}}{\partial t}+\left(\widetilde{\boldsymbol{u}}\cdot\nabla\right)\widetilde{\boldsymbol{u}}+\frac{1}{\rho}\nabla\widetilde{p} \;=\nu\nabla^2\widetilde{\boldsymbol{u}}+\frac{1}{\rho}\widetilde{\boldsymbol{F}}_{el}-\nabla\cdot\boldsymbol{\tau}\,, \tag{3}$$

$$\frac{\partial\widetilde{\rho}_{\mathrm{el}}}{\partial t}+\widetilde{\boldsymbol{u}}\cdot\nabla\widetilde{\rho}_{\mathrm{el}} \;=D\nabla^2\widetilde{\rho}_{\mathrm{el}}-\frac{\sigma}{\epsilon}\widetilde{\rho}_{\mathrm{el}}-\nabla\cdot\boldsymbol{\zeta}\,, \tag{4}$$

$$\nabla^2\widetilde{\phi} \;=\;-\frac{\widetilde{\rho}_{\mathrm{el}}}{\epsilon}\,. \tag{5}$$

In the above system, $\widetilde{\boldsymbol{u}}=(\widetilde{u},\widetilde{v},\widetilde{w})$ and $\widetilde{p}$ stand respectively for the filtered fluid velocity and dynamic pressure, while $\rho$ and $\nu$ denote the fluid density and kinematic viscosity. Also, $\widetilde{\rho}_{\mathrm{el}}$ and $\widetilde{\phi}$ are the filtered electric-charge density and electric potential. In other words, $\widetilde{\boldsymbol{E}}=-\nabla\widetilde{\phi}$ with $\widetilde{\boldsymbol{E}}$ being the filtered electric field. Further, $\sigma$, $\epsilon$ and $D$ are, respectively, the electric conductivity, electric permittivity and ionic diffusivity of the fluid. For the problems of interest these quantities can be assumed to be constant; see relevant discussion in Calero et al. (2023).

Assuming that the absolute values of the valences of anions and cations are equal, the electric charge density is defined by,

$$\rho_{el} \;=\; e_0 z(n_{\mathrm{P}}-n_{\mathrm{N}})\,, \tag{6}$$

where $e_0$ is the elementary charge, $z$ the absolute ionic valence and $n_{\mathrm{P}}$ and $n_{\mathrm{N}}$ the concentrations of cations and anions, respectively. Also, the electric conductivity, i.e. the inverse of the resistivity, is defined by,

$$\sigma \;=\; \frac{e_0^2 D n_0}{k_{\mathrm{B}}T}\,, \tag{7}$$

where $n_0=n_{\mathrm{P}}+n_{\mathrm{N}}$ is the total ionic concentration, $k_{\mathrm{B}}$ the Boltzmann constant, and $T$ the temperature. It is also worth adding that the Debye length, $\lambda_{\mathrm{D}}$, is defined as, $\lambda_{\mathrm{D}}=\sqrt{\frac{\epsilon k_{\mathrm{B}}T}{e_0^2 n_0}}$ (Paillat et al., 2001b). By virtue of the definition (7) of the electric conductivity, this expression becomes,

$$\lambda_{\mathrm{D}} \;=\; \sqrt{\frac{\epsilon\, D}{\sigma}}\,. \tag{8}$$

In other words, the Debye length is proportional to the square root of the resistivity, as mentioned in the Introduction.

In the momentum equation (3), the forcing term $\widetilde{\boldsymbol{F}}_{el}$ is the filtered Lorentz force, i.e. the volumetric electric force acting on the fluid. Also in (3), the residual tensor $\boldsymbol{\tau}$ represents the unclosed terms of the filtered momentum equation (3),

$$\boldsymbol{\tau} \;=\; \widetilde{\boldsymbol{u}\,\boldsymbol{u}} - \widetilde{\boldsymbol{u}}\,\widetilde{\boldsymbol{u}}\,, \tag{9}$$

and has to be modeled. $\boldsymbol{\tau}$ can be interpreted as an additional, turbulent stress tensor. With regard to notation, the term $\boldsymbol{u}\,\boldsymbol{u}$ denotes the dyadic product of $\boldsymbol{u}$ with itself.

Similarly, the residual vector $\boldsymbol{\zeta}$ represents the unclosed terms of the filtered charge-density equation (4),

$$\boldsymbol{\zeta} \;=\; \widetilde{\rho_{\mathrm{el}}\boldsymbol{u}} - \widetilde{\rho}_{\mathrm{el}}\,\widetilde{\boldsymbol{u}}\,. \tag{10}$$

and has to be modeled as well. This residual vector can be interpreted as an additional turbulent flux.

In the problems of interest, the relevant hydrodynamic dimensionless group is the Reynolds number. Our study is concerned with electrification in turbulent channel flows and it is therefore convenient to introduce the friction Reynolds number $Re_\tau = u_\tau h/\nu$, where $h$ is the half-width of the channel and $u_\tau$ is the friction velocity. The latter one is defined as $u_\tau = \sqrt{\tau_{\mathrm{w}}/\rho}$ with $\tau_{\mathrm{w}}$ being the wall shear stress. Also, the dimensionless groups related to charge transport are the electric Schmidt number, $Sc = \nu/D$, and the ratio between the hydrodynamic and electrostatic time scales $r_{\mathrm{t}} = (h/u_\tau)/(\epsilon/\sigma)$. The ratio $\epsilon/\sigma$ appears in the ohmic-resistance term of (4) and is commonly referred to as the charge relaxation time.

The literature on subgrid-scale modeling for the Navier Stokes equations is vast; see, for example, (Pope, 2000; Sagaut, 2005; Ferziger et al., 2019) and references therein. The most common approach is to introduce the eddy-viscosity concept according to which $\boldsymbol{\tau}$ is represented as an additional viscous stress-tensor. Then, we have,

$$\boldsymbol{\tau} - \frac{1}{3}\mathrm{tr}(\boldsymbol{\tau})\boldsymbol{I} \;=\; -2\nu_{\mathrm{t}}\widetilde{\boldsymbol{S}}\,, \tag{11}$$

where $\mathrm{tr}(\boldsymbol{\tau})$ is the trace of $\boldsymbol{\tau}$, $\boldsymbol{I}$ the identity tensor and $\widetilde{\boldsymbol{S}}$ the filtered strain-rate tensor,

$$\widetilde{\boldsymbol{S}} = \frac{1}{2}\left(\nabla\widetilde{\boldsymbol{u}} + \left(\nabla\widetilde{\boldsymbol{u}}\right)^{\top}\right). \tag{12}$$

Typically, the eddy viscosity $\nu_{\mathrm{t}}$ is assumed to scale linearly with the amplitude of the strain rate, i.e.

$$\nu_{\mathrm{t}} \;=\; \left(C_{\mathrm{S}}\,\Delta\right)^2 \sqrt{\widetilde{\boldsymbol{S}} : \widetilde{\boldsymbol{S}}}\,, \tag{13}$$

where the double dot denotes the double inner product between two 2nd-order tensors, $C_{\mathrm{S}}$ is the so-called Smagorinsky coefficient and $\Delta$ the nominal filter size. In this work, $\Delta$ is given by,

$$\Delta \;=\; (\Delta x\,\Delta y\,\Delta z)^{1/3}\,, \tag{14}$$

with $\Delta x$, $\Delta y$ and $\Delta z$ being the dimensions of a given computational cell.

For the sake of simplicity and reduction of computational cost, we have used a constant value for Smagorinsky coefficient. More precisely, we set $C_{\mathrm{S}} = 0.17$, which is the value proposed by Lilly (1992) for channel flows. It is well established that $C_{\mathrm{S}}$ is not constant but depends on the type of problems; see, for example (Canuto and Cheng, 1997). Different values for the Smagorinsky coefficient are available in the literature but typically they range between 0.1 and 0.2; see, for instance, (Deardorff, 1970; Canuto and Cheng, 1997; Pope, 2000; Sagaut, 2005) and references therein. To correct the behavior of the eddy viscosity in the near-wall regions, it is common to add in (13) the van Driest damping function (Pope, 2000). This approach was also adopted in our study. Accordingly, the eddy viscosity reads,

$$\nu_{\mathrm{t}} \;=\; \left(0.17\,\Delta\left(1 - \mathrm{e}^{-y^+/25}\right)\right)^2 \sqrt{\widetilde{\boldsymbol{S}} : \widetilde{\boldsymbol{S}}} \tag{15}$$

where $y^+$ is the distance from the wall measured in wall units, $y^+ = yRe_\tau/h$. Validation tests of the proposed LES model for the flows of interest, consisting of comparisons between LES and direct numerical simulations (DNS), can be found in Calero (2023).

Alternatively, one could employ a dynamic procedure for the computation of the eddy viscosity, such as the popular dynamic model of Germano et al. (1991). In this work we opted for a damping function to adjust $C_S$ for the purposes of simplicity and also to avoid the extra computational cost associated with a dynamic procedure. Furthermore, according to the comparisons between LES and DNS for channel flows presented iin Calero (2023), this approach gave satisfsactory results.

With regard to the modeling of $\widetilde{\boldsymbol{F}}_{el}$, we remark that, for constant emissivity, the Lorentz force is given by $\boldsymbol{F}_{el} = \rho_{el}\boldsymbol{E}$. Therefore, $\widetilde{\boldsymbol{F}}_{el} = \widetilde{\rho_{el}\boldsymbol{E}}$. Earlier numerical studies (Calero et al., 2022, 2023) have shown that in the flows of interest the Lorentz force is very weak. Accordingly, it can be approximated simply by,

$$\widetilde{\boldsymbol{F}}_{el} \approx \widetilde{\rho}_{el}\widetilde{\boldsymbol{E}}\,. \tag{16}$$

Finally, the turbulent flux $\boldsymbol{\zeta}$ is approximated via the so-called gradient assumption,

$$\boldsymbol{\zeta} = -D_t\boldsymbol{\nabla}\widetilde{\rho}_{el}\,. \tag{17}$$

In the above equation, $D_t$ stands for the ionic eddy diffusivity. Modeling options for $D_t$ are discussed in section 4 below.

The governing system (2)-(4) is integrated numerically via the algorithm proposed by Calero et al. (2022). The hydrodynamic component, i.e. the Navier-Stokes equations, is solved via a SIMPLE-based scheme (Ferziger et al., 2019). Whereas, the discretization of the Poisson equation (5) for the electric potential leads to a linear system that is solved via Jacobi iterations. Finally, the charge-density equation is integrated numerically via an upwind method. The combined algorithm has been parallelized using the Message Passing Interface (MPI) protocol and implemented in a Cartesian mesh with a staggered-grid arrangement. Validation tests for the combined algorithm and full details for its implementation are available in (Calero et al., 2022; Calero, 2023). It is also worth adding that this algorithm is part of pafiX (2019), which is an open-source computational tool for electrohydrodynamics.

## 3. Numerical setup

The computational domain consists of a channel with half-width $h = 0.5$ cm. The channel is periodic in the streamwise $x$ and spanwise $z$ directions. The cross-stream direction is then parallel to the $y$ axis. The midplane of the channel is located at $y = 0$.

The working dielectric liquid is benzene at room temperature and its properties are listed in Table 1. The electrical conductivity $\sigma$ is particularly low, as is the case for several liquid hydrocarbons, and its precise value depends on the concentration of impurities. The value listed in Table 1 is the one measured in the experiments of (Forster, 1962). The value of $D$ is calculated via the Einstein-Stokes formula, $D = k_B T/(3\pi\nu\rho d)$ with $d$ being the presumed diameter of the impurities (Ohshima and Furusawa, 1998). In other words, $D$ can vary from one case to another. For the value listed in Table 1, we assumed that $d = 4$ nm, which is deemed to be a reasonable estimate. Given the above values of $D$ and $\sigma$, the Debye length is estimated at $\lambda_D \approx 5.73 \times 10^{-5}$ m. This estimate is within the range of Debye lengths for liquid hydrocarbons mentioned in the works of Touchard et al. (1996) and Cabaleiro et al. (2008).

In our study we consider flows at 4 different friction Reynolds numbers: $Re_\tau = 180$, 210, 300 and 395. The corresponding flow rates are sufficiently high for the thickness of the hydrodynamic boundary layer to be comparable to that of the diffuse layer. Accordingly, flow electrification takes places in all the cases presented herein. Moreover, for the given value of $h$ and range of $Re_\tau$, it can be inferred that the charge-relaxation time $\epsilon/\sigma$ is much larger than the largest hydrodynamic time scale, $h/u_b$ with $u_b$ being the bulk velocity. This means that, in all cases, turbulent fluctuations are expected to play a significant role in the redistribution of charges in the flow domain.

For $Re_\tau = 180$ and 210 the length and depth of the channel are: $L_x = 4\pi h$ and $L_z = 2\pi h$, respectively. Whereas for computational savings, in the cases of $Re_\tau = 300$ and 395 we set $L_x = 2\pi h$ and $L_z = \pi h$. In the high $Re_\tau$ cases, the extent of the channel in the periodic directions have been reduced for purposes of computational savings; nonetheless these dimensions are still sufficiently large so as to prevent spurious interactions between the resolved turbulent structures and to accurately compute the statistical properties of the flow (Lessani and Nakhaei, 2013).

The simulations presented herein are wall-resolved LES, which means that the fluid structures in the near-wall regions, including the boundary layer, are fully resolved. To this end, the distance of the center of the first computational cell from the adjacent wall, $y^+_{fp}$, satisfies $y^+_{fp} < 1$. For example, for the case of $Re_\tau = 180$, this distance was $y^+_{fp} = 0.1$. The width $\Delta y$ of the computational cells is then increased away from the walls and towards the midplane

**Table 1**
Material properties of benzene at 298.15 K.

| Quantity | Source | Value |
|---|---|---|
| $\rho$ | (Chemical-Book, 2022) | 874 Kg/m$^3$ |
| $\nu$ | (Reid et al., 1987) | $6.95 \times 10^{-7}$ m$^2$/s |
| $\epsilon$ | (Brown et al., 1951) | $2.01 \times 10^{-11}$ F/m |
| $\sigma$ | (Forster, 1962) | $1.1 \times 10^{-12}$ S/m |
| $D$ | (Ohshima and Furusawa, 1998) | $1.8 \times 10^{-10}$ m$^2$/s |

**Table 2**
Properties of the computational meshes. $L_x$, $L_y$ and $L_z$ are the channel dimensions, and $N_x$, $N_y$ and $N_z$ are the number of grid points in the respective directions. $\Delta x^+$ and $\Delta z^+$ are the uniform cell spacings in the $x$ and $z$ directions. $\Delta y^+_{\max}$ is the largest grid spacing in the $y$ direction (at the midplane).

| $Re_\tau$ | $L_x \times L_y \times L_z$ | $N_x \times N_y \times N_z$ | $\Delta x^+$ | $\Delta z^+$ | $\Delta y^+_{\max}$ |
|---|---|---|---|---|---|
| 180 | $4\pi h \times 2h \times 2\pi h$ | $96 \times 65 \times 80$ | 23.56 | 14.14 | 8.71 |
| 210 | $4\pi h \times 2h \times 2\pi h$ | $96 \times 65 \times 80$ | 27.48 | 16.49 | 10.16 |
| 300 | $2\pi h \times 2h \times \pi h$ | $96 \times 65 \times 96$ | 19.63 | 9.81 | 14.49 |
| 395 | $2\pi h \times 2h \times \pi h$ | $128 \times 96 \times 128$ | 19.38 | 9.70 | 12.92 |

following a hyperbolic tangent distribution. Nonetheless, in all cases, care has been taken so that a sufficient number of computational cells is placed inside the boundary layers. On the other hand, the grid spacing in the periodic directions is uniform. The summary of the properties of the computational meshes is given in Table 2.

It is worth adding that, another popular approach is the so-called wall-modeled LES. According to it, the flow structures near the walls are not resolved but are modeled. This approach offers considerable computational savings because it allows for the coarsening of the computational mesh in the near-wall regions; see, for example Sagaut (2005). Wall models are based on available approximations of the stucture of the boundary layers. Reliable approximations for the hydrodynamic layer have been developed long ago. However, much less is known about the structure of the boundary layer of the charge density and, therefore, wall models for it are currently unavailable. For this reason, the option of wall-modeled LES has not been pursued herein.

In our simulations, the Stern layers are not resolved because their thickness is at the order of the ion size; instead, for purposes of computation of the electric charge density, they are assumed to be part of the solid wall-liquid interface. Then at the solid boundaries we prescribe the no-slip condition for the velocity and a non-zero Dirichlet condition for the electric charge density $\rho_{el}$. In other words, the electric charge density in the Stern layers is assumed to remain constant; see also the relevant discussion in Abedian and Sonin (1982). More specifically, the charge density at the walls is set to $\rho_{el} = 10^{-4}$ C/m$^3$. Further, a zero-Neumann condition is applied for the electric potential at the top and bottom walls.

In terms of initial conditions, we first perform a preliminary simulation of turbulent channel flow in absence of electric charge. Once the flow becomes fully developed, we then apply the initial profile for the electric charge density and start the simulation of flow electrification. In the cross-stream $y$ direction, the initial charge density consists of an exponentially decreasing profile, starting with the (dimensionless) value of unity at the wall and decreasing so that approximately 95% of the initial charge is located within 3 Debye lengths. This choice was based on the analytical solution for $\rho_{el}$ in laminar channel flow (Calero et al., 2023), according to which 95% of the charge in the diffuse layer is located between the Stern layer and a distance of $3\lambda_D$ from the wall; the same estimate had also been suggested earlier by Paillat et al. (2001b). With this choice, the thickness of the initial charge-density profile corresponds to the actual thickness of the diffuse layer of an EDL for the presumed $\lambda_D$. On the other hand, this profile is constant in the $x$ and $z$ directions. For all the simulations presented therein, we determine the time step via the Courant-Friedrichs-Lewy

(CFL) condition (Ferziger et al., 2019) with the Courant number set to 0.25.

In the next two sections we present results for the mean (time and area-averaged) charge density $\langle \rho_{el} \rangle$, its rms $\rho_{el,rms}$, and the area-averaged charge density at the midplane $\langle \rho_{el} \rangle_{xy}$. These results have been non-dimensionalized by the value at the wall $\rho_w$. Similarly, the coordinate $y$ has been non-dimensionalized by the channel half-width $h$, and the time variable $t$ by $h/u_\tau$.

## 4. Comparison of different models for the ionic eddy diffusivity

As mentioned above, the ionic eddy diffusivity $D_t$ has to be modeled. It is worth noting that the charge density is not a passively advected scalar, due to the presence of the ohmic-resistance term in the corresponding transport equation and its filtered version (4). For this reason it is deemed useful to explore different options for the modeling of $D_t$. In the present study, we have examined four different models and assessed their efficiency. These are the following.

Model 1: zero ionic eddy diffusivity. This is essentially the no-model approach which assumes that the ionic eddy diffusivity is zero, $D_t = 0$. According to this approach the effect of the unresolved turbulent fluctuations of $\rho_{el}$ is not taken directly into account. In the past, some authors advocated this approach for the eddy viscosity $\nu_t$; see, for example, (Oran and Boris, 1991; Fureby and Grinstein, 1999). The underlying idea is that the numerical dissipation due to the discretization of the governing equations can sufficiently take into account the effect of the unresolved turbulent structures.

Model 2: constant ionic eddy diffusivity. According to this approach, the ionic diffusivity is assigned a constant non-zero value. In our study we have tested various values and the one that gave the most satisfactory results turned out to be $D_t = 10^{-9}$ m$^2$/s.

Model 3: estimation via a damping function. In the first two models the eddy diffusivity attains the same value everywhere in the flow domain. However, this is clearly a drawback because the turbulence intensity is not uniform. For example, it is vanishing as we approach the wall but attains high values in the bulk of the channel. One way to alleviate this drawback is by introducing a damping function. Such a function can be derived on the basis of the profiles of the mean (time and area-averaged) charge density $\langle \rho_{el} \rangle$ across the channel computed from DNS. As mentioned in the introduction, DNS results for channel flow electrification at $Re_\tau = 180$ and 210 have been presented in (Calero et al., 2023). On the basis of these results, the expression for $D_t$ involving the damping function is

$$D_t = K \left( 1 - \exp\left( -\frac{y^+}{13} \right) \right)^5 , \tag{18}$$

where $K$ is a coefficient. Numerical tests that we conducted in the framework of our study have shown that a suitable value for it is $K = 7 \times 10^{-6}$ m$^2$/s. It is straightforward to verify that, according to this model, $D_t$ is zero at the wall and increases monotonically until the midplane. The main shortcoming of this approach is that the value of $K$ is not universal and is expected to depend on the Reynolds number and the type of liquid.

Model 4: estimation via a turbulent Schmidt number. This is the most common approach for the estimation of the eddy diffusivity of a passively advected scalar (Lesieur and Rogallo, 1989; Sagaut, 2005). According to it, the eddy diffusivity is associated to the eddy viscosity via the introduction of the turbulent (electric) Schmidt number,

$$Sc_t = \frac{\nu_t}{D_t} . \tag{19}$$

Since $\nu_t$ vanishes as we approach the wall, then so does $D_t$. The value of $Sc_t$ is typically estimated via comparisons with DNS results. In the case of passively advected scalars such as species concentrations, the values of $Sc_t$ range from 1 to 6 (Donzis et al., 2014). On the other hand, when the advected scalar is the temperature, the values of the equivalent turbulent Prandtl number range between 0.4 and 1.2 (Métais and Lesieur, 1992; Kobayashi et al., 1984, 1985; Georgiou and Papalexandris, 2018; Hay and Papalexandris, 2021). Numerical tests that we conducted in the framework of our study showed that for the flows of interest, the estimate that yielded the best comparisons with DNS is $Sc_t = 4$.

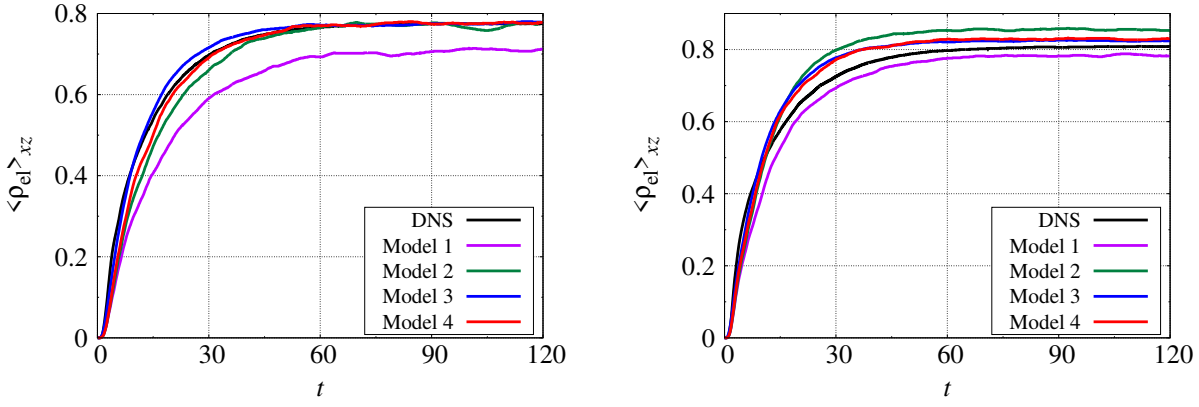
Next we compare the predictions of these four modeling approaches for the ionic eddy diffusivity $D_t$ with the DNS results of flow electrification of benzene at $Re_\tau = 180$ and 210. For the DNS at $Re_\tau = 180$ the grid dimensions are $192 \times 129 \times 225$ grid cells. Whereas for the DNS at $Re_\tau = 210$ they are $280 \times 181 \times 225$ grid cells. In both cases, the DNS mesh is uniform in the $x$ and $z$ directions. In the $y$ direction, the DNS mesh is refined in the near-wall regions

in a fashion similar to that of Kim et al. (1987). More specifically, the $y$ coordinates of the edges of the computational cells are given by the general formula,

$$y_j \;=\; h\,\cos\left(\frac{j-1}{N-1}\pi\right)\,, \qquad j=1,\ldots N\,, \tag{20}$$

where $N$ represents the total number of grid cells in the cross-stream direction. *A* posteriori analysis of the results showed that the ratio of the cell size $\Delta$ to the local Kolmogorov scale was always smaller than 2 everywhere in the computational domain, which confirms the fineness of the employed DNS meshes.

In Figure 1 we have plotted the temporal evolution of the area-averaged charge density $\langle\rho_{\rm el}\rangle_{xz}$ at the midplane ($y=0$) for the two values of $Re_\tau$ considered herein. This quantity is representative of the electrification of the fluid in the bulk of the channel. As mentioned by Calero et al. (2023), the electrification process consists of 3 stages. In the first stage the electric charge in the bulk of the channel increases very rapidly and at an almost constant rate, i.e. linearly. In the second stage, referred to as the transition stage, the electrification rate slows down which means that the Ohmic resistance becomes progressively more significant. In the third and final stage, $\langle\rho_{\rm el}\rangle_{xz}$ has reached its peak value and remains more or less constant. Therefore, in the final stage, the charge-density distribution is statistically stationary and the convective charge transport counterbalances the Ohmic resistance.



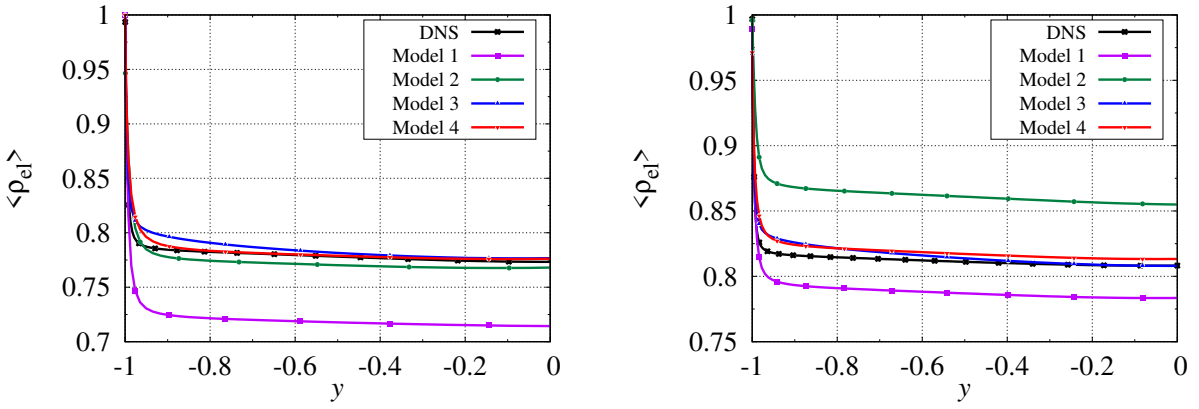

(a) $Re_\tau = 180$. (b) $Re_\tau = 210$.

**Fig. 1:** Comparison between DNS and LES profiles of the temporal evolution of the area-averaged charge density $\langle\rho_{\rm el}\rangle_{xz}$ at the midplane ($y=0$).

From the plots of Figure 1, we readily infer that, at $Re_\tau = 180$, model 1 underestimates significantly the values of $\langle\rho_{\rm el}\rangle_{xz}$ at all three stages of evolution. At $Re_\tau = 210$, it also underestimates $\langle\rho_{\rm el}\rangle_{xz}$ but to a lesser extent. Whereas, model 2 yields satisfactory predictions at $Re_\tau = 180$ but it overestimates $\langle\rho_{\rm el}\rangle_{xz}$ at $Re_\tau = 210$. On the other hand, the predictions of models 3 and 4 are considerably more accurate and very close to one another. At $Re_\tau = 180$ both models predict correctly the initial electrification rate and the peak value of $\langle\rho_{\rm el}\rangle_{xz}$. Nonetheless, model 3 slightly overestimates $\langle\rho_{\rm el}\rangle_{xz}$ during the second stage of evolution. Also, at $Re_\tau = 210$, models 3 and 4 slightly overpredict the peak value. Overall, the predictions of models 1 and 2 for $\langle\rho_{\rm el}\rangle_{xz}$ are not sufficiently accurate. Models 3 and 4 yield satisfactory predictions, with the performance of model 4 being slightly superior to that of model 3.

Next we discuss the predictions of the aforementioned models for the mean and rms charge density across the channel, $\langle\rho_{\rm el}\rangle$ and $\rho_{{\rm el},rms}$ respectively. Statistics are taken during the final stage of the evolution process, i.e. once the electrification is completed and the charge-density distribution has become statistically stationary. The sampling period is 80 flow-through times, $L_x/u_{\rm b}$, with $u_{\rm b}$ being the bulk velocity.

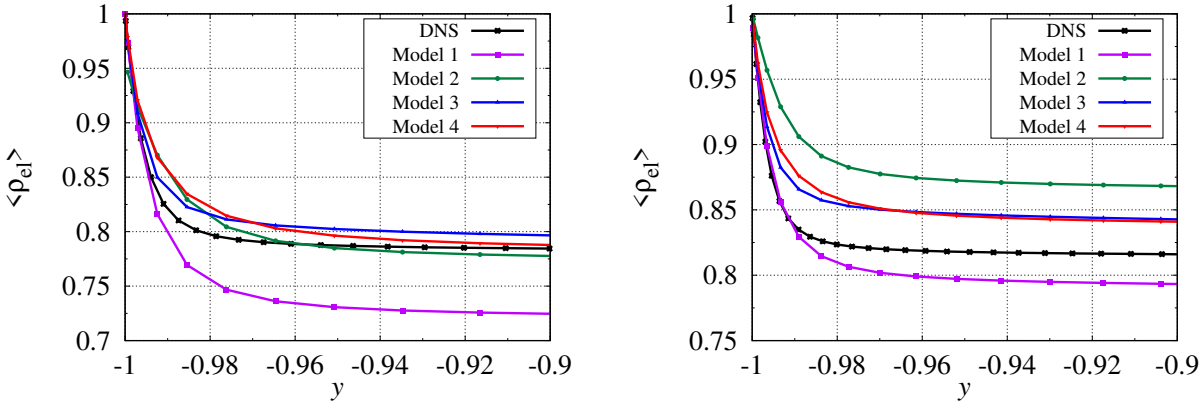
Profiles of $\langle\rho_{el}\rangle$ at $Re_\tau = 180$ and 210, as predicted by the DNS and the LES, are shown in Figure 2. Also, in Figure 3 we provide a zoom of these profiles near the wall. From these plots we readily infer that, once again, model 1 underestimates significantly the values of the charge density, especially at $Re_\tau = 180$. Model 2 yields satisfactory predictions at $Re_\tau = 180$ but overestimates considerably $\langle\rho_{el}\rangle$ at $Re_\tau = 210$.




(a) $Re_\tau = 180$. (b) $Re_\tau = 210$.

**Fig. 2:** Comparison between DNS and LES profiles of the mean charge density $\langle \rho_{\mathrm{el}} \rangle$ across the channel.

On the contrary, the predictions of models 3 and 4 are again much more accurate. At $Re_\tau = 180$ these models approximate satisfactorily the profile both in the near-wall regions and in the bulk of the flow. Actually, at $Re_\tau = 180$, model 4 is slightly more accurate across the channel but at $Re_\tau = 210$ model 3 gives slightly better predictions near the midplane.



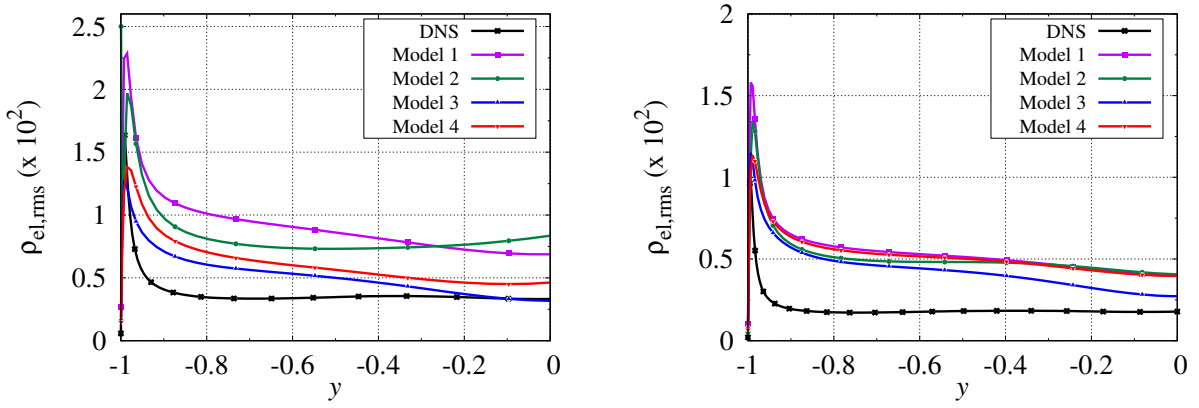

(a) $Re_\tau = 180$. (b) $Re_\tau = 210$.

**Fig. 3:** Zoom of the predicted profiles for the mean charge density $\langle \rho_{\mathrm{el}} \rangle$ near the wall.

Plots of the rms of the charge density, $\rho_{\mathrm{el},rms}$, across the channel are provided in Figure 4. Also, zoom of these profiles near the wall is provided in Figure 5. Globally, the LES profiles of $\rho_{\mathrm{el},rms}$ are less accurate than those of the mean charge density. This, however, is expected since rms profiles are second-order statistics. Further, from these plots we infer that model 1 overpredicts significantly $\rho_{\mathrm{el},rms}$, especially at $Re_\tau = 180$. Similarly, model 2 overestimates significantly the rms values. Moreover, model 2 predicts a spurious non-zero value at the wall and a spurious local peak at the midplane.

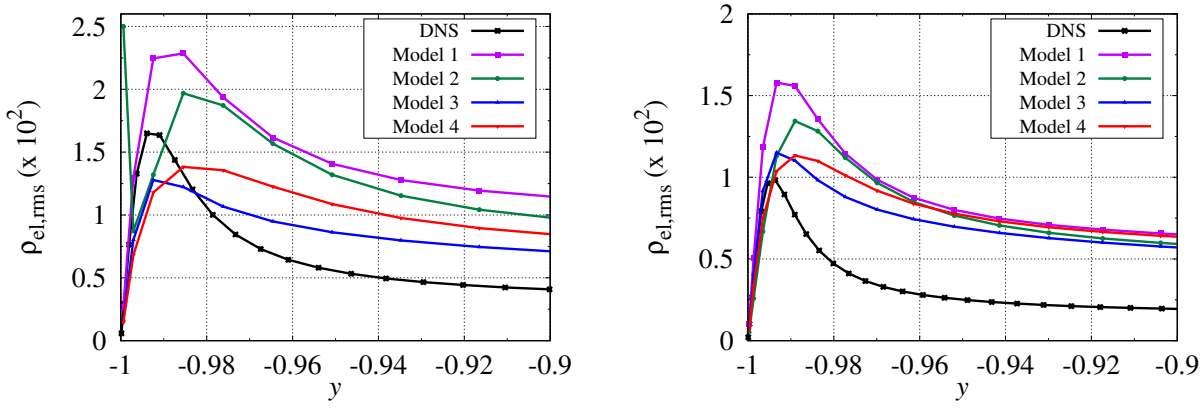
On the other hand, the errors of the models 3 and 4 are smaller, especially at $Re_\tau = 180$. In particular, they provide better estimates of the peak rms values in the near-wall regions. Also, their predictions for the rms profiles in the bulk are closer to the DNS values. It is also worth noting that at $Re_\tau = 210$, the $\rho_{\mathrm{el},rms}$ predictions of model 3 are more accurate than those of model 4.

In summary, models 1 and 2 resulted in significant inaccuracies. On the contrary, models 3 and 4 provided satis-




(a) $Re_\tau = 180$. (b) $Re_\tau = 210$.

**Fig. 4:** Comparison between DNS and LES profiles of the rms of the electric charge density, $\rho_{el,rms}$, across the channel.




(a) $Re_\tau = 180$. (b) $Re_\tau = 210$.

**Fig. 5:** Zoom of the profiles for $\rho_{el,rms}$ near the wall.

factorily accurate predictions. Overall, the levels accuracy of models 3 and 4 are comparable. However, model 4 is easier to implement and does not require calibration of any parameter, whereas the coefficient $K$ in model 3 is flow-dependent. Moreover, model 4 has the additional advantage of explicitly relating the subgrid-scale fluctuations of $\rho_{el}$ with those of the velocity via the introduction of $\nu_t$. For this reason, we have opted for model 4 in our LES study of flow electrification at higher $Re_\tau$.

It is worth adding that instead of a constant turbulent Schmidt number, one could employ a dynamic procedure for calculating its value. This case is equivalent to that of passively advected scalars; therein one can use either a constant value for the turbulent Prandtl (or Schmidt) number or compute it dynamically. However, this approach is not used very often in practice because it increases the computational complexity and cost. For this reason, it has not been considered in the present study. Nonetheless we plan to examine its efficacy in future studies.

It is also interesting to add that the comparisons between LES and DNS confirmed that the magnitude of the Lorentz force is exceedingly small and that the approximation (16) of its filtered version is sufficiently accurate. The smallness of the Lorentz force implies that in the flows examined herein the electric charge does not affect the fluid motion or the turbulence statistics. This is partially due to the fact that the prescribed charge density at the walls is quite small. Nonetheless, this is a rather special case; under the presence of electric fields, there are many flows in which the Lorentz force plays an important role.

## 5. LES results of channel-flow electrification

In this section we present results obtained from LES for electrification of liquid benzene during channel flow. As mentioned above, we consider four different friction Reynolds numbers, $Re_\tau = 180$, 210, 300 and 395. All results presented in this section have been obtained with model 4 for the turbulent eddy diffusivity, i.e. via a turbulent Schnmidt number.

The evolution of the average charge density at the midplane, $\langle \rho_{\rm el} \rangle_{xz}$, is plotted in Figure 6. In all cases, the electrification process consists of three stages, as outlined by Calero et al. (2023): the initial rapid build-up of charge (high electrification rate), a transition stage (lower electrification rate) and the statistically stationary stage which signals the completion of electrification. As expected, the electrification rate increases substantially with the turbulence intensity. For example, at $Re_\tau = 395$, the working medium (liquid benzene) attains the third stage of electrification approximately three times faster than it does at $Re_\tau = 180$. This is due to the fact that as the turbulence intensity increases, the thickness of the boundary layer decreases and, therefore, there are more turbulent structures that enter the diffuse layer and transport charges towards the bulk of the channel.

Similarly, the peak value of $\langle \rho_{\rm el} \rangle_{xz}$ also increases with $Re_\tau$. For instance, at $Re_\tau = 300$ the final (peak) value of $\langle \rho_{\rm el} \rangle_{xz}$ is 12.3% higher than the one at $Re_\tau = 210$. However, at high $Re_\tau$ this increase becomes much less pronounced. For example, the final value of $\langle \rho_{\rm el} \rangle_{xz}$ at $Re_\tau = 395$ is only 2.7% higher than the one at $Re_\tau = 300$.

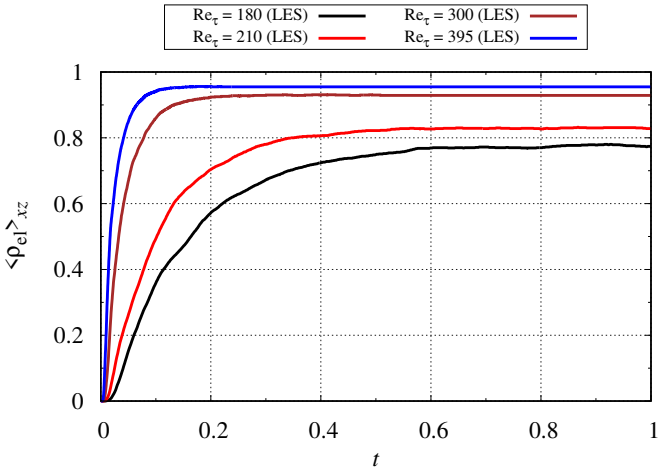



**Fig. 6:** Temporal evolution of the area-averaged charge density $\langle \rho_{\rm el} \rangle_{xz}$ at the midplane ($y = 0$) for the friction Reynolds numbers considered herein.

It is also interesting to observe that for $Re_\tau = 180$ and 210, the average charge at the midplane $\langle \rho_{\rm el} \rangle_{xz}$ exhibits some low-frequency and small-amplitude oscillations in the final stage of the electrification process, i.e. in the statistically stationary state. These oscillations have also been observed at lower Reynolds numbers (Calero, 2023). Their amplitude progressively decreases with $Re_\tau$. More specifically, at $Re_\tau = 300$ these oscillations have all but disappeared. The presence of these oscillations at low $Re_\tau$ is attributed to the convective term in the charge density equation (4), i.e. to the local misalignment of the velocity vector and the charge gradient. Their amplitude diminishes at high $Re_\tau$ because as the turbulence intensity increases, the mixing of electric-charge carriers becomes more efficient, thereby reducing the fluctuations of $\rho_{el}$.

We proceed to discuss the variation of the total charge and streaming current with the turbulence intensity. The total charge $Q$ is simply the integral of the charge density over the entire flow domain. In the case of a channel with dimensions $L_x \times 2h \times L_z$ the corresponding relation reads,

$$Q = 2 \int_0^{L_x} \int_{-h}^{0} \int_0^{L_z} \rho_{\rm el} \, dz \, dy \, dx \, . \tag{21}$$

Another quantity that is useful for comparisons is the electric charge inside the diffuse layers, $Q_{\rm DL}$. The thickness of

the diffuse layer is denoted by $\gamma$. Accordingly, $Q_{\mathrm{DL}}$ is given by,

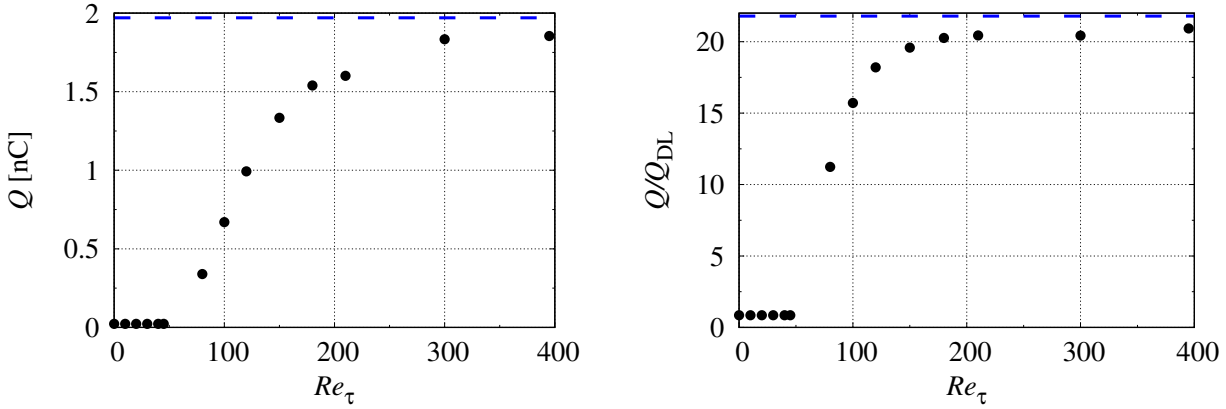
$$Q_{\mathrm{DL}} = 2\int_0^{L_x}\int_{-h}^{-h+\gamma}\int_0^{L_z} \rho_{\mathrm{el}}\, dz\, dy\, dx\,. \tag{22}$$

According to the analytical solution for $\rho_{el}$ in laminar channel flow (Calero et al., 2023), more than 98% of the charge inside the diffuse layer lies within a distance of 4 Debye lengths. It can therefore be assumed that the thickness of the diffuse layer is equal to 4 Debye lengths, i.e. $\gamma \approx 4\lambda_{\mathrm{D}}$.

In the case of laminar flow in a channel, no electrification takes place because, under the assumption of negligible Lorentz force, the liquid velocity is everywhere perpendicular to the gradient of the charge density: $\boldsymbol{u}\cdot\nabla\rho_{el} = 0$. Therefore, the charge distribution is the same as when the fluid is at rest. More specifically, in this case the electric charge is confined within the diffuse layer, i.e. in laminar flows we have that $Q_{\mathrm{DL}} = Q$. Therefore, comparison between $Q_{\mathrm{DL}}$ and $Q$ provides a direct measure of the electric charge that has been transported in the flow domain due to the turbulent motions of the fluid.

The variation of the total charge $Q$ and the ratio $Q/Q_{\mathrm{DL}}$ with the friction Reynolds number are shown in Figures 7a and 7b, respectively. From these plots we readily reaffirm that when the channel flow is laminar, then the electric charges are confined inside the diffuse layers adjacent to the channel. However, once the flow enters the transition regime $Re_\tau > 50$, then both $Q$ and $Q/Q_{\mathrm{DL}}$ increase monotonically. In the same figures we can observe that the increase rate of $Q$ and $Q/Q_{\mathrm{DL}}$ is initially quite fast. However, the increase rate becomes slower at higher $Re_\tau$.

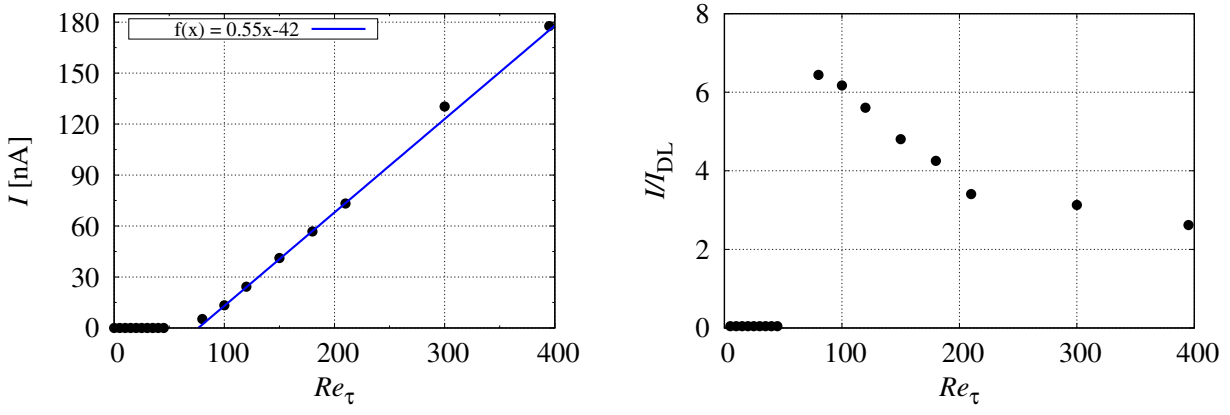
In the Figures 7a and 7b we have also plotted the corresponding values at the theoretical upper limit of flow electrification. This limit corresponds to infinite Reynolds number and zero boundary-layer thickness. At this limit, the charge density is equal to the value at the wall everywhere in the flow domain. Accordingly, the limit value of the total charge in the channel is $2hL_xL_z\rho_{\mathrm{w}}$. Given the domain dimensions and the boundary value ($\rho_{\mathrm{w}} = 10^{-4}$ C/m$^3$), this theoretical limit is equal to 1.97 nC. In an analogous manner, the theoretical limit of the ratio $Q/Q_{\mathrm{DL}}$ is equal to $h/\gamma$, which in our case is equal to 21.81. It is important to note that this upper limit is purely theoretical and cannot be attained in practice. This is due to the ohmic resistance and the presence of hydrodynamic boundary layers Nonetheless, it represents a state of reference that is useful for comparison purposes. According to the plots of Figure 7, the total charge $Q$ is quite close to this upper limit when $Re_\tau \geq 300$.




(a) Total charge $Q$. (b) Ratio $Q/Q_{\mathrm{DL}}$.

**Fig. 7:** Variation of the total charge $Q$ (a) and the ratio $Q/Q_{\mathrm{DL}}$ with the friction Reynolds number. The data points for $Re_\tau = 300$ and 395 are from LES while the other ones are from DNS (Calero, 2023). The horizontal dashed lines represent the theoretical limits when the charge density is equal to $\rho_{\mathrm{w}}$ everywhere in the domain. Since the LES at $Re_\tau = 300$ and 395 have been conducted at a smaller domain, the values shown herein are the computed values multiplied by the ratio of the domain size.

Another important parameter for flow electrification is the streaming current $I$. This is the current of electric




(a) Streaming current $I$. (b) Ratio $I/I_{\mathrm{DL}}$.

**Fig. 8:** Variation of the total streaming current $I$ (a) and the ratio $I/I_{\mathrm{DL}}$ (b) with the friction Reynolds number. The data points for $Re_\tau = 300$ and 395 are from LES while the other ones are from DNS (Calero, 2023). Since the LES at $Re_\tau = 300$ and 395 have been conducted at a smaller domain, the values shown herein are the computed values multiplied by the ratio of the domain size.

charges due to the motion of the fluid parallel to the wall, i.e. due to the fluid stream, and is given by,

$$I = \frac{1}{h}\int_0^{L_x}\int_{-h}^{0}\int_0^{L_z} \rho_{\mathrm{el}} u \, dz \, dy \, dx \,, \tag{23}$$

where $u$ is the streamwise component of the fluid velocity. In an analogous manner, the streaming current confined in the diffuse layer is given by,

$$I_{\mathrm{DL}} = \frac{1}{\gamma}\int_0^{L_x}\int_{-h}^{-h+\gamma}\int_0^{L_z} \rho_{\mathrm{el}} u \, dz \, dy \, dx \,. \tag{24}$$

When the liquid is at rest, the streaming current is zero. On the other hand, in laminar flows in a channel, the electric charges are confined inside the diffuse layers but are advected by the flow in the direction parallel to the walls. Therefore, even at laminar flows, the streaming current is non-zero. Evidently, in laminar flows, $I = I_{\mathrm{DL}}$. Whereas in turbulent flows, $I > I_{\mathrm{DL}}$. As mentioned in the Introduction, the development of strong streaming currents has been considered the precursor of several industrial fires and explosions due to static electricity (Klinkenberg and van der Minne, 1958; Ohsawa, 2011).

Plots of the variation of the streaming current $I$ and the ratio $I/I_{\mathrm{DL}}$ are provided in Figures 8a and 8b, respectively. In the same figure, we have juxtaposed a fit of the streaming current, derived via the nonlinear least-squares Levenberg-Marquardt algorithm. This fit reads,

$$I\left(Re_\tau\right) \approx C_1 Re_\tau + C_2 \,, \qquad \text{for} \quad Re_\tau \geq 100 \,. \tag{25}$$

with $C_1 = 5.5 \times 10^{-10}$ A and $C_2 = -4.2 \times 10^{-8}$ A. According to these plots, the streaming current is constant at laminar flows and increases almost linearly with $Re_\tau$ in the transitional and turbulent regimes, up to $Re_\tau = 395$. With regard to the ratio $I/I_{\mathrm{DL}}$, we readily observe that it equals unity in the laminar regime, as expected. However, as soon as the flow becomes transitional, this ratio jumps to a high value and then decreases with $Re_\tau$. In other words, as the turbulence intensity increases, the relative contribution of the streaming current from the bulk of the domain is reduced.

Next, we present the predictions of our LES for the first and second-order statistics of the charge density. As before, the sampling period is 80 flow-through times. In Figure 9 we have plotted the profiles of the mean charge density, $\langle \rho_{\mathrm{el}} \rangle$, across the channel for the four values of $Re_\tau$ considered herein. Overall, the shape of the profiles is the same as that predicted by the DNS at low turbulence intensities of Calero et al. (2023). More specifically, the $\langle \rho_{\mathrm{el}} \rangle$ profiles consist

of three zones. The first one is adjacent to the wall and inside both the hydrodynamic boundary layer and the diffuse layer. Within this zone, the fluid velocity is exceedingly small and the dominant mechanism of transport of charge is the ionic diffusion. Its thickness is a couple of percentage points of the unit length (the channel half-width $h$). In the second zone, convective transport of charge becomes important and, therefore, the competing mechanisms therein are the convective and conductive currents. This zone terminates at a distance of 0.10 to 0.15 unit lengths from the wall. Finally, the third zone is characterized by a very slow decrease of the charge density away from the walls. From the plots of Figure 9 we can also infer that an increase of the turbulence intensity reduces the thicknesses of the first and second zones and also uniformizes the charge-density distribution away from the walls.

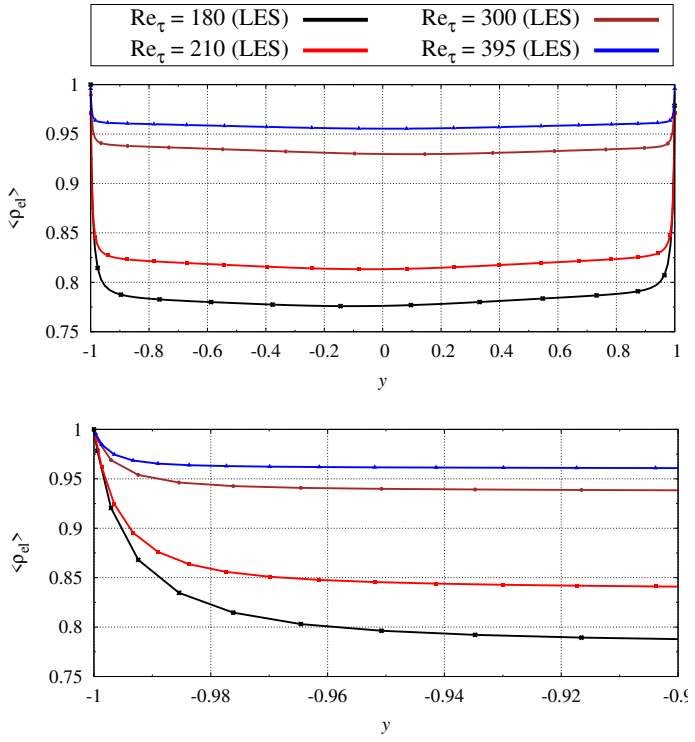



**Fig. 9:** Top: profiles of the mean charge density, $\langle\rho_{\mathrm{el}}\rangle$, across the channel. Bottom: zoom of the profiles near the wall.

Finally, results for the rms of the charge density, $\rho_{\mathrm{el,rms}}$, across the channel are provided in Figure 10. Once again, the shape of these profiles are the same as those predicted by DNS at lower turbulence intensities. In particular, the rms values exhibit a strong peak near the wall and then drop in the bulk of the channel. This peak coincides with the end of the first zone mentioned above. The location of the peak moves closer to the wall as $Re_\tau$ increases, i.e. the thickness of the first zone of the $\langle\rho_{\mathrm{el}}\rangle$ profile becomes smaller. Additionally, the values of $\rho_{\mathrm{el,rms}}$ across the channel decrease as $Re_\tau$ increases. As already mentioned above, this is due to the fact that mixing is enhanced as the turbulence intensity increases. The same trend is also observed in passively advected scalars in turbulent flows; for example, in free convection the rms of the (normalized) temperature decreases as the turbulence becomes more intense (Hay and Papalexandris, 2019, 2020).

It is also interesting to observe that in the bulk of the channel the predicted rms profiles are not flat but exhibit some very small variations. This is most likely a numerical artifact due to the subgrid-scale modeling. Nonetheless, the amplitude of this variation is very low, from which we may infer that overall the performance of the subgrid-scale model is satisfactory.

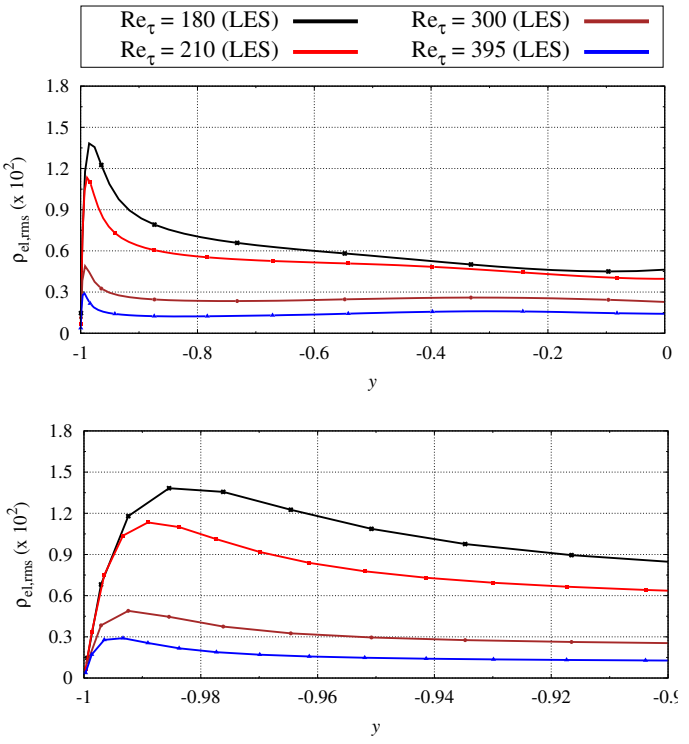



**Fig. 10:** Top: profiles of the charge density rms, $\rho_{\mathrm{el,rms}}$, across the channel. Bottom: zoom of profiles near the wall

## 6. Conclusions

In this paper we have studied electrification of liquid dielectrics in channel flows of moderate turbulence intensities via large eddy simulations. Accordingly, we first derived the filtered version of the governing equations. The unclosed terms in the momentum equation are approximated by the eddy-viscosity model that incorporates a constant Smagorisnky coefficient and the van Driest damping function. Similarly, the unclosed term in the charge-density equation are modeled via the eddy diffusivity approach, i.e. they are represented as a turbulent flux that captures the effect of the subgrid-scale fluctuations of the charge density. This additional flux involves the so-called eddy ionic diffusivity, $D_{\mathrm{t}}$. In our study we examined and assessed the accuracy of 4 models for $D_{\mathrm{t}}$. The models based on zero or constant eddy ionic diffusivity resulted in significant inaccuracies. On the contrary, the models based on a damping function and on the turbulent electric Schmidt number yielded unsatisfactory results. In our simulations we then opted for the model based on the turbulent Schmidt number, because of its simplicity and robustness.

Our simulations predicted that both the electrification rate and the overall charge increase monotonically with the turbulence intensity. Additionally, the streaming current increases almost linearly with the friction Reynolds number $Re_\tau$. The electrification process consists of three stages, namely, the initial build-up of charge in the channel, the transition stage, and the statistically stationary stage in which the charge in the channel remains constant. We have also confirmed that in the last stage the mean charge-density profile consists of three zones. The first one is dominated by charge diffusion of the wall and the second one by increased convective current. The third zone is characterized by a very slow decrease of the charge density away from the walls. As expected, the first zone becomes thinner as the turbulence intensity increases. At the same time, the rms value of the charge density become smaller due to enhanced turbulent mixing. In the future we plan to perform simulations at even higher Reynolds number and also extend our studies in pipe and duct flows.

## 7. Acknowledgements

The first and third authors gratefully acknowledge the financial support of the National Research Fund of Belgium (FNRS) under the FLOW-CHARGE grant.The second author gratefully acknowledges the financial support from the European Research Council (ERC) under the European Union's Horizon 2020 research and innovation programme (grant agreement No. 947606 PowFEct).

## References

Abedian, B., Sonin, A., 1982. Theory for electric charging in turbulent pipe flow. J. Fluid Mech. 120, 199–217.

Atkins, P., de Paula, J., Keeler, J., 2018. Atkins' Physical Chemistry. 11th ed., Oxford University Press, London.

Berg, J.C., 2010. An introduction to Interfaces and Colloids. World Publishing.

Boumans, A., 1957a. Streaming current in turbulent flows and metal capillaries. i. theory (1). distribution of charge in the liquid. Physica XXIII 23, 1007–1026.

Boumans, A., 1957b. Streaming current in turbulent flows and metal capillaries. ii. theory (2). charge transported by the flow of liquid. Physica XXIII 23, 1027–1037.

Boumans, A., 1957c. Streaming current in turbulent flows and metal capillaries. iii. experiment (1). aim and procedure. Physica XXIII 23, 1038–1046.

Boumans, A., 1957d. Streaming current in turbulent flows and metal capillaries. iii. experiment (2). results and conclusions. Physica XXIII 23, 1047–1055.

Bourgeois, A., Paillat, T., Moreau, O., Mortha, G., Touchard, G., 2005. Flow electrification in power transformers: salt-type additive as a potential remedy? J. Electrostat. 63, 877âĂŞ882. 10th International Conference on Electrostatics.

Brown, A.S., Levin, P., Abrahamson, E., 1951. Dielectric Constant of Benzene at 25Âřc by the Wyman Method. J. Chem. Phys. 19, 1226–1229.

Cabaleiro, J., Paillat, T., Artana, G., Touchard, G., 2019. Flow Electrification in Turbulent Flows of LiquidsâĂŤComparison of Two Models for One Specific Case. IEEE Trans. Ind. Appl. 55, 5235–5328.

Cabaleiro, J., Paillat, T., Moreau, O., Touchard, G., 2008. Flow electrification of dielectric liquids in insulating channels: Limits to the application of the classical wall current expression. J. Electrostat. 66, 79–83.

Calero, M., 2023. Flow Electrification of Dielectric Liquids: Modeling and Numerical Study. Doctoral Dissertation, UCLouvain.

Calero, M., Grosshans, H., Papalexandris, M., 2022. A computational framework for electrification of liquid flows. J. Loss Prevent. Proc. 74, 104637.

Calero, M., Grosshans, H., Papalexandris, M., 2023. Electrification in turbulent channel flows of liquid dielectrics. Phys. Fluids 35, 045119.

Canuto, V., Cheng, Y., 1997. Determination of the SmagorinskyâĂŞLilly constant $C_S$. Phys. Fluids 9, 1368–1378.

Chemical-Book, 2022. https://www.chemicalbook.com/.

Deardorff, J.W., 1970. A numerical study of three-dimensional turbulent channel flow at large Reynolds numbers. J. Fluid Mech. 41, 453–480.

Domínguez, G., Touchard, G., 1997. Streaming current development in a rectangular channel. J. Electrostat. 40-41, 153–159. Proceedings of the 8th International Conference on Electrostatics.

Donzis, D., Aditya, K., Sreenivasan, K., Yeung, P., 2014. The turbulent Schmidt number. J. Fluids Eng. - T. ASME 136, 060912–1.

El-Adawy, M., Paillat, T., Bertrand, Y., Moreau, O., Touchard, G., 2010. Physicochemical Analysis at the Interface Between Conductive Solid and Dielectric Liquid for Flow Electrification Phenomenon. IEEE Trans. Ind. Appl. 46, 1593–1600.

El-Adawy, M., Paillat, T., Touchard, G., 2011. Numerical simulation of the electrical double layer development: Physicochemical model at the solid and dielectric liquid interface for laminar flow electrification phenomenon. IEEE Trans. Dielectr. Electr. Insul. 18, 1463–1475.

Ferziger, J.H., Perić, B., Street, R., 2019. Computational Methods for Fluid Dynamics. 4th ed., Springer.

Forster, E., 1962. Electric Conduction in Liquid Hydrocarbons. I. Benzene. J. Chem. Phys. 37, 1021–1028.

Fureby, C., Grinstein, F., 1999. Monotonically integrated large eddy simulation of free shear flows. AIAA J. 37, 544–556.

Gavis, J., Koszman, I., 1961. Development of charge in low-conductivity liquids flowing past surfaces: A theory of the phenomenon in tubes. J. Colloid Sci. 16, 375–391.

Gavis, J., Wagner, J., 1968. Electric charge generation during flow of hydrocarbons through microporous media. Chem. Eng. Sci. 23, 381–391.

Georgiou, M., Papalexandris, M.V., 2018. Direct numerical simulation of turbulent heat transfer in a t-junction. J. Fluid Mech. 845, 581âĂŞ614.

Germano, M., Piomelli, U., Moin, P., Cabot, W., 1991. A dynamic subgrid-scale eddy viscosity model. Phys. Fluids 3, 1760–1765.

Hay, W., Papalexandris, M., 2019. Numerical simulations of turbulent thermal convection with a free-slip upper boundary. Proc. Roy. Soc. A. 475, 20190601.

Hay, W., Papalexandris, M., 2020. Evaporation-driven turbulent convection in water pools. J. Fluid Mech. 904, A14.

Hay, W., Papalexandris, M., 2021. Turbulent thermal convection driven by free-surface evaporation in cuboidal domains of different aspect ratios. Phys. Fluids 33, 015104.

Huber, P.W., Sonin, A.A., 1977a. Electric charging in liquid hydrocarbon filtration: A comparison of theory and experiments. J. Colloid Interface Sci. 61, 126–145.

Huber, P.W., Sonin, A.A., 1977b. Theory for electric charging in liquid hydrocarbon filtration. J. Colloid Interface Sci. 61, 109–125.

Kim, J., Moin, P., Moser, R., 1987. Turbulence statistics in fully developed channel flow at low Reynolds number. J. Fluid Mech. 177, 133–166.

Klinkenberg, A., 1959. Le Mouvement d'Ãľlectricité accompagnant le Mouvement des Liquides et sa Conséquence, l'Ãľlectricité dite Statique. G. Chim. 82, 149–157.

Klinkenberg, A., 1964. Elektrische Aufladung schlecht leitender FlÃijssigkeiten bei turbulenter StrÃűmung. Chem. Ing. Tech. 36, 283–290.

Klinkenberg, A., van der Minne, J., 1958. Electrostatics in the petroleum industry. 1st ed., Elsevier Publishing Company, University of Minnesota.

Kobayashi, T., Kano, M., Ishihara, T., 1984. Prediction of turbulent flow in two-dimensional channel with turbulence promoters (1st report, numerical predictions by large eddy simulation). Bull. JSME 27, 1893–1898.

Kobayashi, T., Kano, M., Ishihara, T., 1985. Prediction of turbulent flow in two-dimensional channel with turbulence promoters (3rd report, improvement of large eddy simulation and formation of streaklines). Bull. JSME 28, 1893–1898.

Koszman, I., Gavis, J., 1962a. Development of charge in low-conductivity liquids flowing past surfaces: Engineering predictions from the theory developed for tube flow. Chem. Eng. Sci. 17, 1013–1022.

Koszman, I., Gavis, J., 1962b. Development of charge in low-conductivity liquids flowing past surfaces: Experimental verification and application of the theory developed for tube flow. Chem. Eng. Sci. 17, 1023–1040.

Leblanc, P., Cabaleiro, J.M., Paillat, T., Touchard, G., 2017. Impact of the laminar flow on the electrical double layer development. J. Electrostat 88, 76–80. Special Issue on The International Conference on Electrostatics.

Leblanc, P., Paillat, T., Cabaleiro, J., Touchard, G., 2018. Flow electrification investigation under the effect of the flow parameters. Int. J. Plasma Environ. Sci. Technol. 11, 156–160.

Lesieur, M., Rogallo, R., 1989. Large-eddy simulation of passive scalar diffusion in isotropic turbulence. Phys. Fluids 1, 718–722.

Lessani, B., Nakhaei, M., 2013. Large-eddy simulation of particle-laden turbulent flow with heat transfer. Int. J. Heat Mass Trans. 67, 974–983.

Lilly, D., 1992. The representation of small-scale turbulence in numerical simulation experiments. IBM Form. 4, 195–210.

Métais, O., Lesieur, M., 1992. Spectral large-eddy simulation of isotropic and stably stratified turbulence. J. Fluid Mech. 239, 157–194.

Ohsawa, A., 2011. Statistical analysis of fires and explosions attributed to static electricity over the last 50 years in japanese industry. J. Phys. Conf. Ser. 301, 1–6.

Ohshima, H., Furusawa, K. (Eds.), 1998. Electrical Phenomena at Interfaces. Fundamentals, Measurements, and Applications. volume 76 of *Surfactant Science*. 2nd ed., Routledge, New York.

Oran, E.S., Boris, J.P., 1991. Computing turbulent shear flows âĂŤ a convenient conspiracy. Comput. Phys. 7, 532–533.

pafiX, 2019. https://www.ptb.de/cms/asep.

Paillat, T., Cabaleiro, J., Romat, H., Touchard, G., 2009. Flow electrification process: the physicochemical corroding model revisited. IEEE Trans. Dielectr. Electr. Insul. 16, 359–363.

Paillat, T., Moreau, E., Grimaud, P., Touchard, G., 2000. Electrokinetic phenomena in porous media applied to soil decontamination. IEEE Trans. Dielectr. Electr. Insul. 7, 693–704.

Paillat, T., Moreau, E., Touchard, G., 2001a. Flow electrification through porous media. J. Loss Prev. Process. Ind. 14, 91âĂŞ93.

Paillat, T., Moreau, E., Touchard, G., 2001b. Space charge density at the wall in the case of heptane flowing through an insulating pipe. J. Electrost. 53, 171–182.

Pope, S.B., 2000. Turbulent Flows. Cambridge University Press, New York.

Reid, R., Prausnitz, J., Poling, B., 1987. The properties of gases and liquids. 4th ed., McGraw-Hill, New York.

Sagaut, P., 2005. Large eddy simulation for incompressible flows: an introduction. Springer Science & Business Media.

Stern, O., 1924. Zur Theorie der Elektrolytischen Doppelschicht. Z. Elektrochem 30, 508–516.

Touchard, G., 1978. Streaming currents developed in laminar and turbulent flows through a pipe. J. Electrostat. 5, 463–476.

Touchard, G., 2021a. Turbulent flow electrification with hydrocarbon liquids, liquid hydrogen, liquefied natural gas (LNG) and liquid nitrogen: Part I–Three different models. Int. J. Plasma Environ. Sci. 15, 1–32.

Touchard, G., 2021b. Turbulent flow electrification with hydrocarbon liquids, liquid hydrogen, liquefied natural gas (LNG) and liquid nitrogen: Part II–Experiments and comparison with different models. Int. J. Plasma Environ. Sci. 15, 1–15.

Touchard, G., Patzek, T.W., Radke, C.J., 1996. A physicochemical explanation for flow electrification in low-conductivity liquids in contact with a corronding wall. IEEE Trans. Ind. Appl. Soc. 32, 1051–1057.

Walmsley, H., Woddford, G., 1981. The generation of electric currents by the laminar flow of dielectric liquids. J. Phys. D: Appl. Phys 14.

Washabaugh, A., Zhan, M., 1997. A chemical reaction-based boundary condition for flow electrification. IEEE Trans. Dielectr. Electr. Insul. 4, 688–709.